Princeton Plasma Physics Laboratory

PPPL-4203
PPPL-4203

Novel Design Methods for Magnetic Flux Loops in NCSX, the National Compact Stellarator Experiment

N. Pomphrey, E. Lazarus, M. Zarnstorff,
A. Boozer, and A. Brooks

December 2006

PPPL
PRINCETON PLASMA
PHYSICS LABORATORY

Prepared for the U.S. Department of Energy under Contract DE-AC02-76CH03073.

Princeton Plasma Physics Laboratory
Report Disclaimers

Full Legal Disclaimer

Trademark Disclaimer

PPPL Report Availability

Princeton Plasma Physics Laboratory:

http://www.pppl.gov/pub_report/

Office of Scientific and Technical Information (OSTI):

http://www.osti.gov/bridge

U.S. Department of Energy:

U.S. Department of Energy
Office of Scientific and Technical Information
P.O. Box 62
Oak Ridge, TN 37831-0062
Telephone: (865) 576-8401
Fax: (865) 576-5728
E-mail: reports@adonis.osti.gov

Novel design methods for magnetic flux loops in NCSX, the National Compact Stellarator Experiment

N. Pomphrey[a], E. Lazarus[b], M. Zarnstorff[a], A. Boozer[c], A. Brooks[a]

[a] *Plasma Physics Laboratory, Princeton University, P.O. Box 451, Princeton, New Jersey*

[b] *Oak Ridge National Laboratory, Oak Ridge, Tennessee*

[c] *Columbia University, New York, NY 10027*

Magnetic pickup loops on the vacuum vessel (VV) can provide an abundance of equilibrium information for stellarators. A substantial effort has gone into designing flux loops for the National Compact Stellarator Experiment (NCSX) [Zarnstorff *et al*., Plasma Phys. Control. Fusion **43** A237 (2001)], a 3-field period quasi-axisymmetric stellarator under construction at he Princeton Plasma Physics Laboratory (PPPL). The design philosophy, to measure all of the magnetic field distributions normal to the VV that can be measured, has necessitated the development of Singular Value Decomposition algorithms for identifying efficient loop locations. Fields are expected to be predominantly stellarator symmetric (SS) - the symmetry of the machine design - with toroidal modenumbers per torus, n, equal to a multiple of 3 and possessing reflection symmetry in a period. However, plasma instabilities and coil imperfections will generate non-SS fields which must also be diagnosed. The measured symmetric fields will yield important information on the plasma current and pressure profile as well as on the plasma shape. All fields that obey the design symmetries could be measured by placing flux loops in a single half-period of the VV, but accurate resolution of non-symmetric modes, quantified by the condition number of a matrix, requires re-positioning loops to equivalent locations on the full torus. A sub-array of loops located along the inside wall of the vertically elongated cross-section was designed to detect $n = 3$ $m = 5$ or 6 resonant field perturbations that can cause important islands. Additional sub-arrays included are continuous in the toroidal and poloidal directions. Loops are also placed at symmetry points of the VV to obtain maximal sensitivity to asymmetric perturbations. Combining results from various calculations which have made extensive use of a database of 2500 free-boundary VMEC equilibria, has led to the choice of 225 flux loops for NCSX, of which 151 have distinct shapes.

I. INTRODUCTION AND OVERVIEW

The National Compact Stellarator Experiment (NCSX) is a 3-field period low aspect ratio ($R/<a> = 4.4$) high-beta ($\beta > 4\%$) quasi-axisymmetric device (effective ripple $< 1.5\%$ at the plasma edge) under construction at the Princeton Plasma Physics Laboratory (PPPL) in partnership with the Oak Ridge National Laboratory (ORNL). The NCSX will be used to acquire physics data needed to evaluate the compact stellarator as a fusion concept and to advance the understanding of 3-D plasmas for fusion and basic science[1,2].

The NCSX magnet system has 18 modular coils, three in each of the six stellarator-symmetric half periods of the device, plus toroidal field coils, poloidal field coils, and helical-field trim coils. The coil arrangement, which is shown in Fig. 1, leads to considerable flexibility in targeting plasma shape and physics properties. The nominal major radius is R = 1.4 m, the magnetic field is in the range B = 1.2 - 2.0 T, and the pulse length is 0.3 - 1.2 s. Plasma heating power up to 12 MW is planned, with 3 MW of neutral beam (NB) heating power implemented early in the experimental program, and additional NB power and radio-frequency heating added later. First plasma is scheduled for 2009.

The interpretation of experimental results in NCSX, as in other stellarators, will require accurate equilibrium reconstruction. Magnetic boundary conditions for the reconstruction will be provided by signals from a variety of plasma diagnostics including $\sim$ 200 in-vessel magnetic field probes providing measurements of the field tangential to the vacuum vessel (VV), 50 flux loops co-wound with all of the independently powered magnets (signals from a subset of these loops will be combined to measure the plasma diamagnetism), 2 Rogowski coils, and $\sim$ 36 flux loops to sense eddy currents in the modular coil support shell. In addition, a comprehensive set of magnetic flux loops will be mounted on the exterior surface of the VV providing measurements of the normal component of the field. A timely design of these loops was required since these will be trapped in the space between the vacuum vessel and the modular coil support shell, a space that will be inaccessible after machine construction is complete[3]. A description of novel concepts in the design of the VV-loops is the main purpose of this paper.

Magnetic signals in NCSX are expected to be predominantly stellarator symmetric (SS), the design symmetry of the device. For this symmetry the field normal to the VV is sinusoidal with with toroidal modenumbers per torus, n, equal to a multiple of 3. However, plasma in-

stabilities and coil imperfections will generate periodicity-breaking (PB) magnetic fields with $n = \pm 1, \pm 2, \pm 4, \pm 5, ...$ as well as cosinusoidal non-SS (NSS) fields. Goals for the NCSX flux loop design include: (a) Loops should be effective in reconstructing both SS and NSS magnetic fields; (b) Loops should be concentrated in regions where the plasma contribution to the total signal is significant (easily detected), and distinguishable from the measured total signal; (c) Loops should be sufficiently numerous to provide adequate spatial resolution of the modes; (d) Loops should be sufficiently large in area to provide a useful signal, yet be consistent with goal (c); (e) A subset of loops should have the capability of resolving $n = 3, m = 5$ or 6 resonant field perturbations. In this paper, we explain how these goals were folded into the NCSX flux loop design, leading to a final arrangement with 225 flux loops at specific locations on the VV torus.

A large database of ~ 2500 SS free-boundary VMEC equilibria[4] was formed incorporating random combinations of a variety of current and pressure profiles. The equilibria provide magnetic signals typical of those that can be expected in NCSX. For a trial set of 100 flux loops that tile the VV surface, the flux through each loop was calculated for each equilibrium and stored as a signal matrix. An algorithm for ranking the flux loops was developed which makes extensive use of the Singular Value Decomposition (SVD) of the signal matrix. The algorithm is based on a variable selection method commonly used in multivariate statistics. Highly ranked diagnostics identify regions of the VV surface that are important for placing designed flux loops.

Normalizing toroidal fields to 1.5T, the average (over the equilibria) magnitude of the normal component of the magnetic field at the VV due to plasma currents, B_n^{plas}, is calculated to be $<$ 0.064 T. Plots of the ratio B_n^{plas}/B_n^{total} subject to the condition $B_n^{plas} > 0.01$ T provide guidance for placement of flux loops that meet design goal (b). A comforting correlation is found between regions of the VV surface that satisfy this condition and regions where trial flux loops are calculated to have high rank by the SVD analysis. As expected, there is a correlation between average signal strength and plasma-to-VV separation distance. Analytic estimates of plasma-to-VV signal attenuation argue for a typical dimension of flux loops to be of order the plasma-to-loop separation distance.

A sub-array of loops was designed to detect $n = 3, m = 5$ or 6 islands. To this end, a 128×128 array of dipoles was uniformly distributed on the VV and a response matrix calculated between individual dipole currents and the radial magnetic field generated on resonant surfaces of a baseline VMEC full-current, full-beta equilibrium. SVD inversion of the response matrix and appropriate

projection onto individual resonant harmonics provides patterns on the VV showing regions where the dipoles are effective in generating magnetic islands. By reciprocity, the effective dipole regions also define the location and size of flux loops that are optimally suited for detecting resonant fields. These are regions along the inside wall of the vertically elongated cross-section of the VV.

To provide a poloidally continuous array of flux loops 16 equally spaced flux loops will be wound on one of the three "spacers" that connect adjacent periods of the VV. Two of these loops surround symmetry points of the VV torus and will be useful for detecting departures from SS. Loops will also be wound around each of the two symmetry points on the remaining two spacers. Additional sub-arrays have been chosen to provide continuous flux loop coverage in the toroidal direction on the inboard and outboard midplanes. Of the loops on these toroidal arrays, six surround symmetry points.

Combining the results from the various analyses, 225 two-turn flux loops were chosen for NCSX. Of this number, 151 have distinct shapes and have the primary function of resolving SS modes. These loops can be placed in one of the six available half-periods of the VV providing essentially complete coverage of that half-period. Since the signal from a loop that is mirror-reflected and/or translated toroidally by ± 1 period is unchanged, loops for detecting SS modes can be distributed to equivalent locations over the full torus without compromising the ability to detect these modes. From the point of view of resolving PB and NSS modes, however, there is no such equivalence and distributing loops over the full torus is essential. Calculations of the condition number (ratio of the largest to smallest singular values) of a matrix of NSS mode signals for various spatial distributions of the flux loops show that scattering all 225 of the loops over all 6 half periods, but sampling each of the 151 SS positions at least once is the preferred choice, and leads to the most robust inversion of the diagnostic signals.

The following sections expand on the above overview.

II. EQUILIBRIUM DATABASE FOR SIGNAL ANALYSIS

A database of $\sim$ 2500 stellarator-symmetric free-boundary VMEC equilibria was generated incorporating random combinations of a wide variety of current and pressure profiles and spanning the range of plasma parameters, coil currents, and shapes that can be achieved in NCSX. Profiles were selected from the output of transport simulations of NCSX discharges[6]. In contrast with

previously reported calculations[7] which analysed the physics flexibility of NCSX, equilibria in the current database were not constrained to be stable to ideal magnetohydrodynamic modes. Figure 2 shows a sample of plasma shapes in the database and plots of selected plasma parameters.

III. SVD, SIGNAL PATTERNS, AND SUPER-DIAGNOSTICS

The computed equilibria were used to determine magnetic signals typical of those that will be obtained in experimental campaigns on NCSX. Measured magnetic field signals result from volumetric equilibrium currents which flow in the plasma region, and currents which flow in the external magnets. It follows from Shafranov and Zakharov's "virtual-casing principle"[8] that an observer in the vacuum region cannot distinguish between volumetric currents which flow in the plasma interior and an equivalent surface current that flows on the plasma-vacuum interface. Equilibria that are magnetically distinguishable therefore correspond to distinct surface current distributions. Distinct surface current distributions equivalent to the volumetric currents generate distinct patterns of magnetic field on the VV (and indeed on any toroidal surface (TS) surrounding the plasma). The number of independent field patterns on the VV will equal the number of independent plasma surface current patterns, although field attenuation and signal-to-noise ratio considerations may cause the number of measurable field patterns, N_{pat}, to be less than this number. The number of plasma profile parameters that can be inferred by magnetic field diagnostics mounted on the VV cannot exceed N_{pat}.

Consider a set of M diagnostics that provide measurerements of the magnetic field at various locations on a vacuum TS, and the collection of diagnostic signals for N equilibria. The formulation that follows does not depend on the type of diagnostic; the data may be ideal point measurements of a single component of the magnetic field at specified locations or the magnetic flux through finite area loops on the TS. In all cases, the data is stored in an $M \times N$ matrix $\mathbf{X}$. Matrix element X_{ij} denotes a measurement by diagnostic i for equilibrium j.

Singular Value Decomposition (SVD)[9–11] provides a useful tool for analysis of the signal matrix $\mathbf{X}$. The SVD of $\mathbf{X}$ is formally defined as the triple matrix product

$$\mathbf{X} = \mathbf{U}\mathbf{W}\mathbf{V}^{\mathbf{T}}. \tag{1}$$

where $\mathbf{U}$ and $\mathbf{V}$ are $M \times N$ and $N \times N$ orthogonal matrices with $\mathbf{U}^{\mathbf{T}}\mathbf{U} = \mathbf{I}$, $\mathbf{V}^{\mathbf{T}}\mathbf{V} = \mathbf{I}$ and $\mathbf{W}$ is

an $N \times N$ diagonal matrix of ordered "singular values" $w_i \equiv W_{ii}$ such that

$$w_1 \geq w_2 \geq \cdots \geq w_N \geq 0. \tag{2}$$

From Eq. (1) it follows that

$$\mathbf{XX^T} = \mathbf{UW^2U^T} \Rightarrow (\mathbf{XX^T})\mathbf{u}_j = w_j^2 \mathbf{u}_j, \tag{3}$$

where $\mathbf{u}_j$ denotes the jth column of matrix $\mathbf{U}$. We see that $\mathbf{u}_j$ is the j'th eigenfunction of the $M \times M$ covariance matrix $\mathbf{XX^T}$ and $\lambda_j = w_j^2$ is the corresponding eigenvalue. The j'th column of $\mathbf{V}$ can similarly be shown to be the jth eigenfunction of the $N \times N$ matrix $\mathbf{X^TX}$, the non-zero eigenvalues of which are identical to those of $\mathbf{XX^T}$. Both $\mathbf{u_j}$ and $\mathbf{v_j}$ "belong" to the same singular value.

Interpretation of the SVD begins with a rewrite of Eq. (1): Any column of $\mathbf{X}$ can be written exactly as

$$\mathbf{x}_k = \sum_{j=1}^{N} \mathbf{u}_j (w_j \mathbf{V}_{kj}) \equiv \sum_{j=1}^{N} \mathbf{u}_j \tilde{X}_{jk}, \tag{4}$$

showing that the signal vector for any one equilibrium in the database is expressed by SVD as a superposition of a common set of independent orthogonal functions, $\mathbf{u}_j$. The $\mathbf{u}_j$ are often called Empirical Orthogonal Functions (EOF's)[12]. The coeffi cients $\tilde{X}_{jk}$ have a magnitude determined by the size of the associated singular value w_j. The $\tilde{X}_{jk}$ are often called Principal Components (PC's)[12,13]. EOF's corresponding to small enough PC values (essentially determined by the magnitude of w_j) contribute insignifi cantly to the structure of the measured signal pattern $\mathbf{x}_k$.

To interpret the EOF's it is convenient to associate the original measurement vector $\mathbf{x}_k$ with a set of unit base vectors:

$$\begin{aligned} \mathbf{x}_k &= [X_{1k}, X_{2k}, \cdots, X_{Mk}]^T \\ &= X_{1k}[1,0,0,\cdots,0]^T + X_{2k}[0,1,0,\cdots,0]^T \\ &+ \cdots + X_{Mk}[0,0,0,\cdots,1]^T \\ &= \sum_{j=1}^{M} \mathbf{e}_j X_{jk}. \end{aligned} \tag{5}$$

Comparing Eq. (5) with Eq. (4) we note a change of basis from the original space of measurements, which employs the trivial unit vectors $\mathbf{e_j}$, to a new set of base vectors $\mathbf{u}_j$. SVD is the

provider of the change of variables:

$$\mathbf{U^T X} = \tilde{\mathbf{X}} = \mathbf{W V^T}. \tag{6}$$

Columns of $\mathbf{U}$ act on columns of $\mathbf{X}$, so each $\mathbf{u}_j$ defines a particular linear combination of measurements. In the next paragraph we will show that among all possible choices of base vectors (linear combinations of diagnostics), $\mathbf{u}_j$ is the choice that recovers the maximum possible variance. It is appropriate to think of the linear combination of diagnostics specified by $\mathbf{u}_j$ as defining a "super-diagnostic"(s-d).

Consider the linear combination of diagnostic signals expressed by $\mathbf{c^T X}$ and choose column vector $\mathbf{c}$ to make $var(\mathbf{c^T X})$ maximal subject to $\mathbf{c^T c} = 1$. The $\mathbf{c}$ that solves this problem is a blending vector that defines a linear combination of diagnostics that explains the greatest possible variance among the measured signals. Finding $\mathbf{c}$ requires maximizing $F(\mathbf{c}) = \mathbf{c^T X X^T c} - \lambda(\mathbf{c^T c} - 1)$ with λ a Lagrange multiplier. The solution is

$$(\mathbf{X X^T})\mathbf{c} = \lambda \mathbf{c}, \tag{7}$$

with λ an eigenvalue of covariance matrix $\mathbf{X X^T}$ and $\mathbf{c}$ the corresponding eigenvector. Maximizing F requires selection of the largest eigenvalue. Comparing Eq. (7) with Eq. (3) we see that among all possible linear combinations of diagnostics, the combination which recovers the maximum variance uses blending vector $\mathbf{c} = \mathbf{u}_1$. From Eq. (6) the fraction of the total variance recovered by this primary s-d is $w_1^2 / \sum_{j=1}^{M} w_j^2$.

A simple extension of the analysis shows that the components of eigenvector $\mathbf{u}_2$ define a second s-d that recovers the greatest possible remaining variance subject to orthogonality between $\mathbf{u}_2$ and $\mathbf{u}_1$. Repetition leads to an ordered set of M s-d's summarized by the transformation $\tilde{\mathbf{X}} = \mathbf{U^T X}$. The k'th s-d recovers $r_k = w_k^2 / \sum_{j=1}^{M} w_j^2$ of the total variance in the measurement data.

Determining the k-value for which $1 - r_k \approx 0$ defines the number of effective signal patterns, N_{pat}.

IV. NUMBER OF MEASURABLE FIELD PATTERNS ON THE VV

To see how much plasma information might be accessible to an efficiently designed magnetic diagnostic system mounted on the VV, let us calculate N_{pat} for the ensemble of equilibria in the

database assuming a dense coverage of field sensors on the VV. A VV toroidal surface (VV-TS), identical to the NCSX VV, but without holes for ports was parameterized by a Fourier representation for major radius R_{VV} and height Z_{VV} as functions of poloidal angle θ and toroidal angle ϕ. For each equilibrium the component of magnetic field normal to the VV-TS was calculated at $M = 1200$ points on a 60×20 uniform mesh of θ, ϕ values using the EXTENDER code[14]. Since each of the $N = 2500$ VMEC equilibria is stellarator symmetric $B_n(\theta, \phi) = -B_n(-\theta, -\phi)$), the mesh spans only one half of one period of the full torus. EXTENDER calculates both $\mathbf{B}^{tot}$ and $\mathbf{B}^{plas}$, the total magnetic field and plasma contribution to the total field, respectively.

From the calculated fields the $M \times N$ signal matrix, $\mathbf{X}$, was computed using the normal component of the external magnetic field, $B_n^{ext} \equiv (\mathbf{B}^{tot} - \mathbf{B}^{plas}) \cdot \hat{\mathbf{n}}$, where $\hat{\mathbf{n}}$ is a unit vector normal to the VV-TS. Figure 3 shows the first thirty singular values of the computed spectrum. The SVD of $\mathbf{X}$ provides $Min(M, N) = 1200$ non-zero singular values. A clear division of the spectrum into two groups of singular values is seen; the first group contains eight singular values, the second group contains the remainder, down in the computational noise associated with the computation of $\mathbf{B}^{plas}$. Such a division is expected: The external field distributions correspond to currents which flow in current carrying circuits external to the plasma. There are eight coil circuits (3 modular coils, 4 poloidal field shaping coils, and 1 toroidal field coil) whose currents vary throughout the database, i.e., there are 8 degrees-of-freedom for the fields due to the coils. The SVD analysis correctly predicts this number. Each singular value corresponds to a particular linear combination of fields from all the coils.

Figure 4 shows the singular value spectrum when the signal matrix $\mathbf{X}$ uses $B_n^{tot} \equiv \mathbf{B}^{tot} \cdot \hat{\mathbf{n}}$, the normal component of the measured total field. Nineteen singular values correspond to measurable field patterns in excess of 1 Gauss (horizontal line in figure). If we regard 1 Gauss, or some such similar value, as a minimum measurable field signal, Fig. 4 shows that variation of plasma profiles and boundary shapes results in a substantial number of measureable field patterns associated with the plasma variation (see, also, previously reported results for the Wendelstein 7-AS stellarator[11]). We have argued in Sec.III that the number of independent signal patterns is likely a measure of the number of profile parameters that can be extracted from the signal data. The aim of the NCSX VV flux loop design effort is to maximize accessibility to available plasma information, subject to engineering constraints.

V. RANKING TRIAL FLUX LOOPS FOR IMPORTANCE

In this section we discuss the use of SVD methods which determine regions of the NCSX VV that are most effective for placing flux loops that identify equilibrium magnetic field patterns. In multivariate statistics these methods are commonly called variable selection techniques[15] and require little modification for the present use.

Fig. 5 is a 3-D view of one of the three periods of the VV torus. A trial set of 100 flux loops was chosen to populate a half-period of the VV-TS. The loops are similar rectangles in a $\theta - \phi$ plane representation of the vessel and are shown in Fig. 6. Grey areas in the figure denote port regions. These are useful here and in later sections for orienting the $\theta - \phi$ plots with respect to 3-D views of the VV. The outboard and inboard midplanes correspond to $\theta = 0^\circ$ and $\theta = \pm 180^\circ$, respectively. The two curves which traverse the figure in the toroidal ϕ-direction mark the top and bottom of the vacuum vessel. Spacer collars connect adjacent periods of the VV. Collar boundaries are shown as curves which traverse the figure in the poloidal θ-direction.

For each of the N equilibria the magnetic flux through each of the $M = 100$ trial loops was calculated using codes V3RFUN and V3POST[5] and stored in an $M \times N$ matrix $\mathbf{X}$. The following procedure for ranking the diagnostics was applied: An SVD on $\mathbf{X}$ is calculated. For EOF $\mathbf{u}_j$ whose singular value is smallest ($j = M$ since the singular values are ordered), we identify the diagnostic i whose $|\mathbf{U}_{ij}|$ is largest. Diagnostic i is removed from the trial set of diagnostics by eliminating row i of $\mathbf{X}$. An SVD of the resulting reduced matrix is calculated. The above operations are repeated for $j = M, M-1, \cdots, 5$ in succession, rejecting for each j that i-labelled diagnostic for which $|\mathbf{U}_{ij}|$ is maximum, and which has not previously been rejected. The 4 diagnostics that remain are permanently placed in a reserve pool. They are the 4 highest ranked diagnostics in the set of M. The entire procedure is repeated, beginning now with an SVD of the $(M-4) \times N$ matrix formed from the original $\mathbf{X}$ by eliminating the 4 rows which correspond to the diagnostics which were placed in the reserve pool. After the second pass of SVD calculations and eliminations are complete, the 4 diagnostics that remain are added to the reserve pool. They are seeded 5-8 in the accumulating ranking list of diagnostics. After completing $M/4$ passes, all M diagnostics have been assigned a rank.

The rationale for the diagnostic rejection method used in the inner loop of the ranking algorithm and known in multivariate statistics as Jolliffe's B2 method[16,17], is that if M diagnostics provide

only $m < M$ independent measurements then $M - m$ linear dependencies exist of the form $\mathbf{c} \cdot \mathbf{x}_j = 0$ where the $\mathbf{c}$ are constant vectors. SVD detects such linear dependencies through Eq (4) in the form of $\mathbf{u}_i \cdot \mathbf{x}_j = w_i \mathbf{V}_{ji}$, so that if singular value w_i is sufficiently small to be considered zero then $\mathbf{u}_i \cdot \mathbf{x}_j = 0$ for all j. Therefore the components of $\mathbf{u}_i$ are the same coefficients as those which express the linear dependencies within the diagnostic set (i.e., $\mathbf{u}_i \equiv \mathbf{c}$ above). A principal component with $w_i = 0$ satisfies $\tilde{\mathbf{X}}_{ij} = \sum_{k=1}^{M} \mathbf{U}_{ki} \mathbf{X}_{kj} = 0$ so that any one of the $\mathbf{X}_{kj}$ for which $\mathbf{U}_{ki} \neq 0$ can be expressed as a linear combination of all other $\mathbf{X}_{mj}$. The $\mathbf{X}_{kj}$ with the largest coefficients are most important in any principal component, therefore choosing k for which $|\mathbf{U}_{ki}|$ is maximum selects the diagnostic most responsible for the small singular value as the diagnostic to be rejected.

The reason for having the outer iteration loop is that having some redundancy of diagnostics is desirable. Imagine there are two diagnostics that provide essentially the same signal information, and the information is crucial for equilibrium reconstruction. A small singular value would result from the near linear dependence, leading to early rejection of one of the two diagnostics. With no outer iteration this diagnostic would be ranked low among the set of 100. Having an outer iteration allows this diagnostic to re-enter the pool and be re-considered for a potentially high seed in the final ranking list.

Figure 7 displays the calculated trial loop ranking. The seeding for each loop (a number from $1 - 100$) is marked at the center of each loop. A low seeding implies a highly valued loop. A graded color-fill scheme is used to aid inspection of seeding trends: Loops that are color-filled red are ranked in the top ten in importance for explaining the variance in signal patterns; orange implies a ranking from $10 - 20$, etc. Blue fill implies a diagnostic is unimportant. The outboard midplane region is generally of low importance, except near the bean and bullet symmetry cross sections ($\phi = 0^\circ$ and $\pm 60^\circ$, respectively). This is fortunate since major ports cut the vessel in this region (see grey areas) limiting the placement of actual loops. Important loops are seen in helical bands crossing the symmetry cross sections. For example two bands cross the bean cross section; one close to the top and bottom of the vessel (loops seeded 6 and 10 are a guide), and the other crossing near the inboard midplane (loops seeded 3 and 5). Another broader band crosses the bullet cross section near the top and bottom of the vessel (loops seeded 1 and 2 are a guide). Generally, the inboard midplane region is important except near the bullet cross section.

VI. RANK CORRELATION WITH VV DISTANCE AND SIGNAL ATTENUATION

There appears to be a good correlation between loop importance (low seeding) and VV-to-plasma separation distance, d_{sep}. Fig. 8 shows a cross section of the plasma and VV at three toroidal angles. A striking feature of this figure is the large d_{sep} for the outboard region of the bean cross section (to provide tangential access for neutral beam injection) and the highly non-uniform dependence of d_{sep} on θ and ϕ, particularly near $\phi = 0$. This may be largely responsible for the observed rapid changes in loop rank over small distances on the VV. Although correlation with d_{sep} is clearly not the sole determinant of loop rank, it is certainly important. The correlation is an indication, as one would expect, that signal attenuation considerations should factor into the actual NCSX flux loop design. In the Appendix we present a simple analytic estimate of signal attenuation, providing an argument that a typical dimension of a flux loop should be of order the plasma-to-loop separation distance.

A goal of the NCSX flux loop design is to maximize the potential for accessing plasma profile information from the magnetic measurements. The measured signal is the total (plasma + coils) magnetic field. One might expect that loops which will prove most useful for distinguishing internal plasma profiles will be loops that are located in regions of the VV where the plasma contribution to the total field is significant. In Fig. 9 we show a plot for each trial loop of $< |B_n^{plas}| > / < |B_n^{tot}| >$ (average plasma to average total normal field at the loop center, average over equilibria). The ratio is color-coded in intervals of 0.1 (red implies a ratio in the range 0.9 - 1.0, orange corresponds to a ratio in 0.8 - 0.9, etc). The magnitude of the average plasma contribution to the normal field varies between 0 and 640 Gauss over the VV surface (toroidal fields for all equilibria were normalized to 1.5 T). Regions of Fig. 9 that are devoid of color-filled loops correspond to regions where the average plasma contribution to the measured normal field is less than 100 Gauss. The region near the outboard midplane extending toroidally from the bean cross section does not satisfy this minimum plasma field criterion. Generally, it can be seen that highly ranked loops are located in regions of the VV where the field ratio is greater than 50%.

VII. FLUX LOOPS FOR RESONANT FIELD DETECTION

In this section we consider the design of dual purpose flux loops that are useful not only in the context of non-resonant equilibrium field identification, but may be useful for aiding the detection of resonant fields that can generate $n = 3, m = 5$ or 6 islands near the $\iota = 0.6$ and $\iota = 0.5$ flux surfaces. To this end, the VV was populated with a 128×128 array of unit dipoles. The field from each dipole was evaluated at the relevant resonant flux surfaces ($\iota = 0.6$ or $\iota = 0.5$) for a baseline VMEC full-current, full-beta equilibrium. The component of the field normal to the resonant surface was Fourier decomposed in magnetic coordinates and a response matrix calculated relating individual dipole currents and resonant components of the field. SVD inversion of this matrix and appropriate projection onto individual resonant harmonics allows construction of bubble plots of B_{mn} for each resonance, providing patterns on the VV showing regions where the dipoles are effective in generating magnetic islands. By reciprocity, these effective dipole regions also define the location and size of flux loops that are optimally suited for detecting resonant fields. Fig. 10 presents a bubble plot for the $n = 3, m = 5$ resonant field corresponding to $\iota = 0.6$. Red corresponds to $B_{mn} > 0$, blue $B_{mn} < 0$. Color intensity is a measure of the magnitude of the field and is greatest between vertical ports near the bean cross section $\phi = 0$. Flux loops for detecting the resonant fields should have a width determined by the separation of contours of $B_{mn} = 0$.

VIII. LOOPS FOR SS MODE DETECTION

Consistent with the results of the foregoing analyses, a strawman flux loop design was developed for detecting SS fields, with loops which cover as much as possible of one half-period of the NCSX VV . This tesselation task is subject to a number of physics and engineering constraints: Loops were chosen to have 2 turns, with a minimum area of $200cm^2$. To take account of the variable plasma-to-vessel separation distance and consequent variable field attenuation, loops were sized according to

$$\text{Loop Area} \sim Max\left(d_{sep}^2, 200\right)[cm^2]. \tag{8}$$

Loops cannot intersect VV port regions; Loop leads are twisted and routed along the VV surface to termination boxes located on the cryostat at the ends of the vertical ports seen in Fig. 5 (seen

as the grey regions near $\theta = \pm 90^\circ$ at $\phi = 0^\circ$ in the center period of Fig. 11). Leads from nearby loops accumulate into wire bundles, and enough space between loops must be allocated to accommodate the bundles. Finally, the resonant field identification loops should be incorporated at the appropriate locations near the inboard midplane.

The result of these considerations is the non-uniform array of 137 flux loops shown as black outline in one half-period of the $\theta - \phi$ plane in Fig. 11). Although the analysis of Sec. VI shows that the loops which straddle the outboard midplane $\theta = 0^\circ$ are not expected to provide important information for SS fields, they are included to provide continuous coverage by loops in both poloidal and toroidal directions. The vertical array of inboard loops nearest the bean cross section at $\phi = 0^\circ$ have a poloidal length scale consistent with the resonant field detection analysis of Sec. VII. Also shown is a continuous poloidal array of 16 equally spaced loops on the VV spacer collar. The representation of these loops is schematic; a detailed design has not yet been made. They are presently envisioned to be $10cm \times 20cm$ rectangular cross section loops, centered as shown. Including the spacer loops, one sees predominantly 7 poloidal and 21 toroidal arrays of loops providing, in principle, the ability to determine stellarator-symmetric modes with poloidal and toroidal modenumbers per period of 11 and 7, respectively.

IX. LOOP PLACEMENT FOR PB AND NSS MODE DETECTION

Magnetic signals are expected to be predominantly stellarator symmetric (SS) with toroidal modenumbers per torus, n, equal to a multiple of 3. For detecting such modes, restricting loops to lie in a single half-period of the machine would be sufficient since SS mode signals are copied into all half-periods. However, plasma instabilities and coil imperfections will generate periodicity-breaking (PB) magnetic fields with $n = \pm 1, \pm 2, \pm 4, \pm 5, \cdots$ and also non-SS (NSS) cosinusoidal modes with $|n| = 3$. The loops shown in red in Fig. 11 show a strawman design for loops which supplement the designed SS loops so that the combined set can be used for periodicity-breaking and NSS mode detection. The NCSX VV has 3 field periods leading to 12 symmetry points on the VV surface at which the normal component of any SS magnetic field vanishes: six lie on the outboard midplane $\theta = 0^\circ$ at $\phi = -120^\circ, -60^\circ, 0^\circ, 60^\circ, 120^\circ, 180^\circ$, and six lie on the inboard midplane $\theta = \pm 180^\circ$ at the same values of ϕ. Accurately constructed stellarator symmetric loops that surround these symmetry points are sensitive detectors of NSS fields and are desirable loops

to include in any design. Also shown in the figure are a poloidally continuous array of 16 loops on a second VV spacer collar, identically wound to those on the first collar, and two toroidally continuous arrays of 15 loops which straddle the inboard and outboard midplanes. The combined set of loops (red and black in the figure) can be used to determine a Fourier mode decomposition of NSS modes. However, the paucity of flux loop coverage in two of the three field periods suggests that the layout of loops shown in Fig. 11 lacks efficiency.

The signal from any one loop that is mirror-reflected in θ, ϕ and/or translated toroidally by ± 1 period is unchanged. Therefore loops for detecting SS modes can be re-distributed to equivalent locations over the full torus without compromising detectability of these modes. To assess the impact on NSS mode detection of various distributions of flux loops, we have calculated the condition number of a response matrix which relates Fourier amplitudes of the normal field at the NCSX VV surface to the measured flux loop signals. The condition number is a measure of the capability to accurately estimate the magnetic field from measurement data in the presence of errors.

Define a response matrix $\mathbf{A}$ with matrix elements

$$A_{ij} = \int\int dS_i \begin{pmatrix} \sin \\ \cos \end{pmatrix} (m_j\theta + n_j\phi), \tag{9}$$

where A_{ij} is the flux through loop i due to a single unit amplitude field harmonic of B_n with poloidal and toroidal modenumbers m_j and n_j, respectively. For M flux loops and N field harmonics matrix $\mathbf{A}$ is $M \times N$. Let $\mathbf{b}$ be an $N \times 1$ vector of Fourier amplitudes of some B_n field at the VV surface:

$$B_n = \sum_{j=1}^{N} b_j \begin{pmatrix} \sin \\ \cos \end{pmatrix} (m_j\theta + n_j\phi), \tag{10}$$

and $\mathbf{c}$ an $M \times 1$ vector of flux loop signals due to some linear combination of B_n field harmonics. Then $\mathbf{b}$ and $\mathbf{c}$ are related through $\mathbf{A}\mathbf{b} = \mathbf{c}$ and determining the field from the measurements requires inverting matrix $\mathbf{A}$. Suppose there is some error, or noise, $\delta\mathbf{c}$ in the flux loop signal vector. It is easy to show[9] that this error leads to a relative error $\|\delta\mathbf{b}\|/\|\mathbf{b}\|$ in the calculated field amplitudes given by

$$\frac{\|\delta\mathbf{b}\|}{\|\mathbf{b}\|} \leq \kappa_A \frac{\|\delta\mathbf{c}\|}{\|\mathbf{c}\|}. \tag{11}$$

Here $\kappa_A = \|\mathbf{A}^{-1}\| \cdot \|\mathbf{A}\| = w_{max}/w_{min}$, the ratio of the largest to smallest singular value of $\mathbf{A}$, is the condition number of matrix $\mathbf{A}$. This ratio of the largest to smallest singular values of $\mathbf{A}$ is

an error amplification factor, expressing the propagation of inaccuracies of known data in $\mathbf{c}$ into greater inaccuracies in the solution $\mathbf{b}$. It is desirable for NSS mode identifi caton to find stellarator symmetric re-distributions of the flux loops shown in Fig. 11 which result in a small κ_A.

To simplify the calculation of κ_A for various loop re-distributions it is convenient to consider a simplified model for the loop geometry. In each frame of Fig. 12 is shown a uniform grid which covers the full torus VV. Cell boundaries represent candidate flux loops. There are 120 cells in each half-period; 20 in the poloidal direction and 6 in the toroidal direction. The 2 poloidal arrays of 16 cells outlined in red represent loop positions on the spacer collars. The 2 toroidal arrays of 15 loops (5 per period) outlined in blue represent loops that span the inboard and outboard midplane. Cells occupied by a star symbol indicate that the flux loop coincident with the enclosing cell boundary is active. The top frame of Fig. 12 shows an array of active loops analogous to the designed loops in Fig. 11 except that stellarator symmetry has been used to replace loops in alternate columns of the half-period $0° < \phi < 60°$ with their mirror images in $-60° < \phi < 0°$. The result is a columnar distribution of loops that occupy alternate columns in one full period (clearly an SS rearrangement that, if applied to Fig. 11, would result in a distribution of loops that would be simpler to install in NCSX than the congested half-period distribution). Two of the three spacer collars have a full complement of 16 loops; the third collar has one loop surrounding each of the two symmetry points. The two sets of 15 loops which straddle the toroidal midplane are also considered active. The bottom frame of Fig. 12 shows a re-distribution of loops where each of the 120 columnar loops was re-positioned to one of six SS-equivalent locations across the entire VV using a random number generator, constrained such that every equivalent symmetrized location is occupied at least once. Additionally, 14 flux loops that were on one of the fully occupied spacer collars were re-assigned at random to unoccupied locations on the full torus, forming 14 SS-duplicates of the previously re-assigned 120. Condition numbers for the two loop distributions of Fig. 12 will be compared.

To evaluate response matrix $\mathbf{A}$ and calculate the condition number determining how well $\mathbf{A}$ can be inverted requires, first, a specification of which modes are considered important enough to be included in the calculation (range of $\mathbf{A}$). We consider NSS modes (cosine and sine) with poloidal and toroidal modenumbers in the range $0 \leq m \leq 3$ and $|n| \leq 3$. The $N = 38$ such modes are sorted in decreasing order of "relevance measure" $r_j = 1/(m_j^2 + n_j^2)$. The condition number for a sequence of $M \times J$ response matrices was evaluated by SVD analysis of the $\mathbf{A}$ matrix which

retains the first $J = 1, 2, \cdots, 38$ modes. Results are shown in Fig. 13.

The solid black and solid red lines in Fig. 13 correspond to the arrayed and irregular distributions of loops shown in the top and bottom frames of Fig. 12. Improved (lower) κ_A is clearly evident for loops that are spread over the full torus compared with the predominantly columnar one period distribution: In the case of the irregular loop distribution, $\kappa_A > 10$ for $J > 21$ modes whereas for the arrayed loops $\kappa_A > 10$ for $J > 12$ modes. For $J = 38$ modes, $\kappa_A \approx 15$ for the irregular distribution, but is 40 times larger for the columnar distribution.

For a given loop distribution the κ_A curves depend on the order in which modes are retained (columns are added to the $\mathbf{A}$ matrix). The curves therefore depend on the choice of relevance measure used to order the modes. The measure used to generate the data for Fig. 13 is an intuitive measure based on mode attenuation. A natural mode order can be defined for a given loop distribution as that order of modes which minimizes the jump between adjacent singular values. To find this natural order we register a sensible mode (e.g., $m = 0, n = 1$) as the first entry in the natural mode table. Then cycle through the remaining modes, identifying the one whose singular value is closest to the first. This mode becomes the second entry in the natural mode table. The procedure continues, identifying one mode at each iteration, each time cycling through all remaining modes. The result is a condition number curve with minimum slope, and the identification of a natural order of modes that are most easily detected by the given flux loops. The black and red dashed curves in Fig. 13 show the result of natural ordering for the columnar and irregular distributions of loops. The dashed curves closely track one another until $J \approx 30$ modes are included after which a substantial improvement is seen for the irregular distribution of loops compared with the columnar distribution. Of course, the end points of each of the solid/dashed curve pairs are equal.

X. FINAL LOOP CHOICE FOR NCSX

Holding the total number of flux loops fixed, several variants of the columnar distribution of loops were investigated for their ability to minimize κ_A. None proved as efficient as the irregular distribution produced by the random number generator. Based on this result, a final layout for flux loops on the NCSX VV was chosen and is shown in Fig. 14. There are a total of 225 two-turn loops distributed over the full torus. To aid visual identification of modenumbers from node counting flux signal data, 16 of these loops are constrained to provide continuous poloidal coverage on one

VV spacer (near $\phi = 60^\circ$ in the figure), and 30 are constrained to form two continuous toroidal arrays of 15 loops around the inboard and outboard midplanes at $\theta = 0^\circ$ and $\theta = \pm 180^\circ$. A vertical array of loops extends between vertical ports near the bean cross section at $\phi = 0^\circ$ to aid measurement of resonant fields, consistent with the analysis of Sec. VII. The remaining loops were randomly distributed over all 6 half-periods of the VV torus, with the constraint that every symmetrized location is occupied at least once. Figure 15 shows a 3-D view of the final flux loop design.

XI. CONCLUSIONS

Relying heavily on linear algebra and especially on various Singular Value Decomposition techniques, an extensive set of magnetic flux loops have been designed for the exterior surface of the NCSX vacuum vessel. The goal was to find an arrangement of loops that can differentiate between measurable magnetic field patterns at the VV. For identification of stellarator-symmetric fields, the flux loops provide the equivalent of complete coverage of one half-period of the VV. To optimize the analysis capability of non stellarator-symmetric magnetic fields, it was found that distributing loops irregularly over all six half-periods of the NCSX VV torus was superior to more traditional arrayed distributions of loops. The installation process was begun in the Fall of 2006.

Appendix 1: Optimal size for magnetic flux loops

A slab model calculation is used to show that the shorter dimension, a, of a highly rectangular magnetic flux loop should be comparable to the distance to the plasma, and the highest wave number that can be resolved is $k = \pi/2a$.

Consider a slab model. The normal magnetic field is $B_x(x,y,z) = B_0 \exp(-kx)\cos(k_y y)\cos(k_z z)$, where $k^2 = k_y^2 + k_z^2$. Suppose a pickup loop is located a distance x from the plasma surface, and the loop is a rectangle of wire that extends over the range $|y| < a/2$ and $|z| < b/2$. The flux through the loop is

$$F(x) = \int_{-a/2}^{a/2} \int_{-b/2}^{b/2} B_x(x,y,z)\,dy\,dz,$$

which implies

$$F(x) = \frac{B_0}{k_y k_z} e^{-kx} \sin(k_y a) \sin(k_z b).$$

The maximum flux is obtained for $k_y a = \pi/2 = k_z b$. Let $L \equiv 1/\sqrt{\frac{1}{a^2} + \frac{1}{b^2}}$ and $A = ab$, then the optimal measured flux is

$$F(x) = \frac{4}{\pi^2} B_0 A \exp(-\frac{\pi}{2}\frac{x}{L}).$$

If $L = x$ the flux is attenuated by a factor of $\exp(\pi/2) = 4.81$ and if $L = x/2$ the flux is attenuated by $\exp(\pi) = 23.14$ for the highest wavenumber that can be reasonably detected, which means

$$k_y \leq \frac{\pi}{2a}, \qquad k_z \leq \frac{\pi}{2b}.$$

Acknowledgements

We are grateful for useful discussions with E. Frederickson, D. Monticello, B. Stratton, G. Labik and T. Brown. We are particularly indebted to M. Drevlak for modifying the EXTENDER code to allow convenient calculation of the magnetic signal matrix on the vacuum vessel, and M. Richman for coding work in the database analysis. This work was supported by the U.S.Department of Energy Contract No.DE-AC02-76-CHO3073

References

[1] M. C. Zarnstorff, L. A. Berry, A. Brooks, *et al*., Plasma Phys. Control. Fusion, **43**, A237 (2001).

[2] G. H. Neilson, A. H. Reiman, M. C. Zarnstorff, *et al*., Phys. Plasmas, **7**, 1911 (2000).

[3] B. Stratton, A. Brooks, T. Brown, *et al*., Rev. Sci. Instruments,**77**, 10E314 (2006).

[4] S. P. Hirshman, and J. C. Whitson, Phys. Fluids, **26**, 3553 (1983).

[5] S. P. Hirshman, E. A. Lazarus, J. D. Hanson, S. F. Knowlton and L. L. Lao, Phys. Plasmas, **11**, 595 (2004).

[6] E. A. Lazarus, M. C. Zarnstorff, S. R. Hudson, *et al*., Fusion Science and Technology, **46**, 209 (2004).

[7] N. Pomphrey, A. Boozer, A. Brooks, *et al*., Fusion Science and Technology, **51** issue 2, page number TBD (2007).

[8] V. D. Shafranov and L. E. Zakharov, Nucl. Fusion, **12**, 599 (1972).

[9] G. Strang, Linear Algebra and its Applications (Academic Press, New York, 1976) 135.

[10] D. Kalman, The College Mathematics Journal, **27**, 2 (1996).

[11] H. P. Callaghan, P. J. McCarthy and J. Geiger, Plasma Phys. Control. Fusion, **42**, 1013 (2000).

[12] R. W. Preisendorfer, Principal Component Analyses in Meteorology and Oceanography (Elsevier, Amsterdam, 1988).

[13] I. T. Jolliffe, Principal Component Analysis (Springer-Verlag, New York, 2002).

[14] M. Drevlak, D. Monticello and A. Reiman, Nucl. Fusion, **45**, 731 (2005).

[15] I. Guyon and A. Elisseeff, Journal of Machine Learning Research, **3**, 1157 (2003).

[16] I. T. Jolliffe, Applied Statistics, **21**, 160 (1972).

[17] J. R. King and D. A. Jackson, Environmetrics, **10**, 67 (1999).

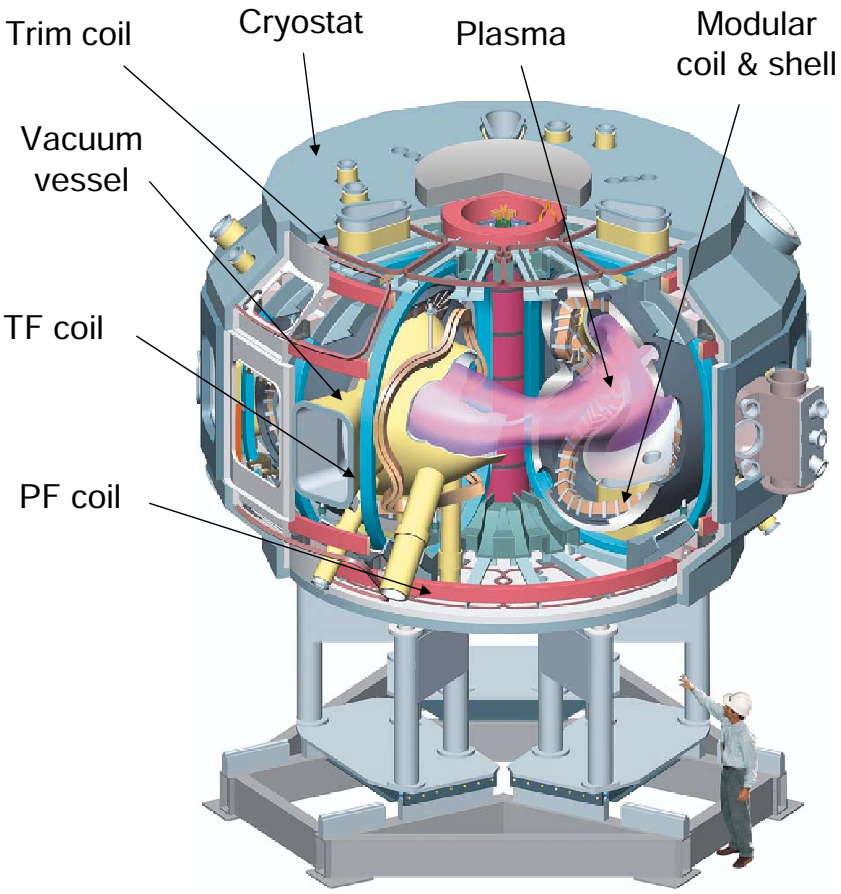

FIG. 1: (Color) NCSX Stellarator Design

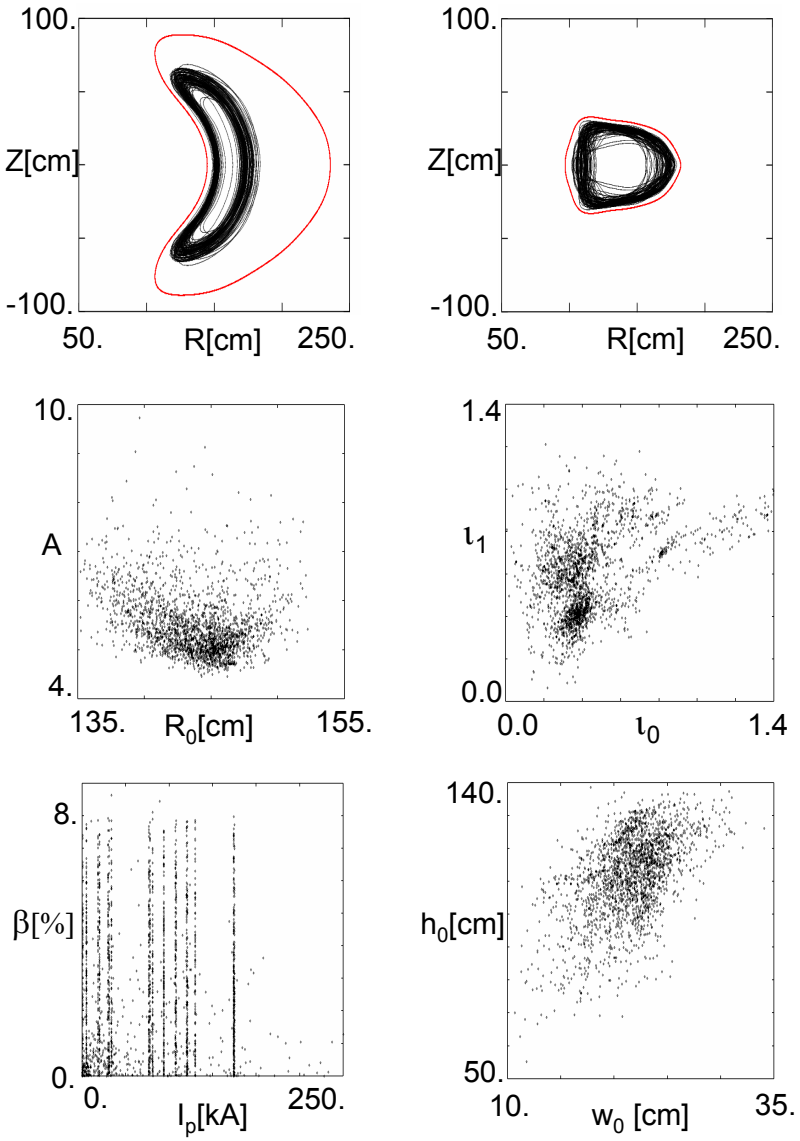

FIG. 2: (Color) Plasma boundaries at the bean ($\phi = 0°$) and bullet ($\phi = \pm 180°$) cross sections for equilibria in the database (first wall boundary in red), and selected plasma parameters for equilibria in database. A = aspect ratio, R_0 = average major radius, ι_1, ι_0 = rotation transform at plasma edge and axis, I_p = plasma current, h_0, w_0 = full height and width at the bean cross section.

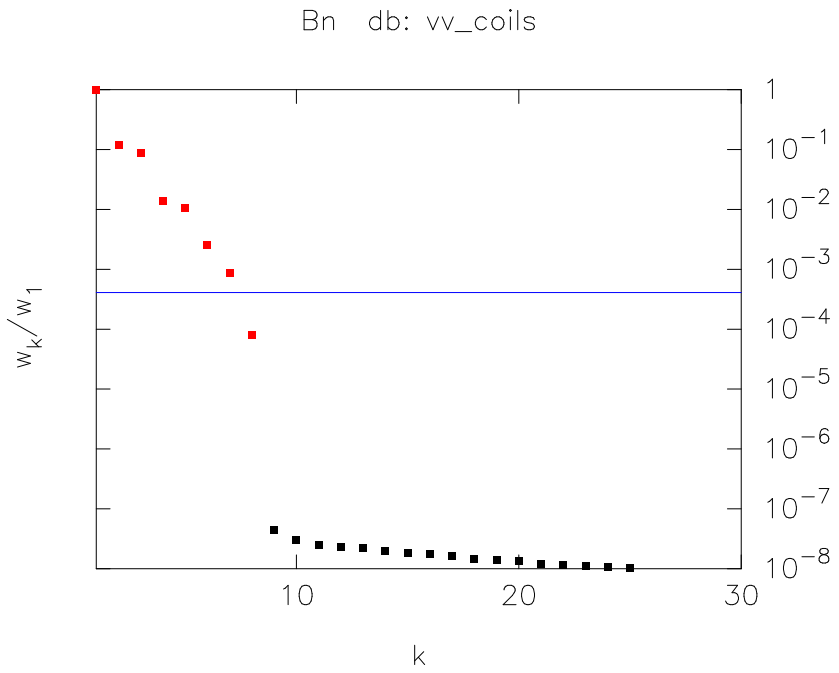

FIG. 3: Singular values, scaled, for an $\mathbf{X}$ matrix which stores B_n^{ext}, the normal component of the external magnetic field on the vacuum vessel. A natural cutoff is seen after the eighth value, consistent with the existence of eight independent coil circuits. The horizontal line corresponds to a field value of 1 Gauss

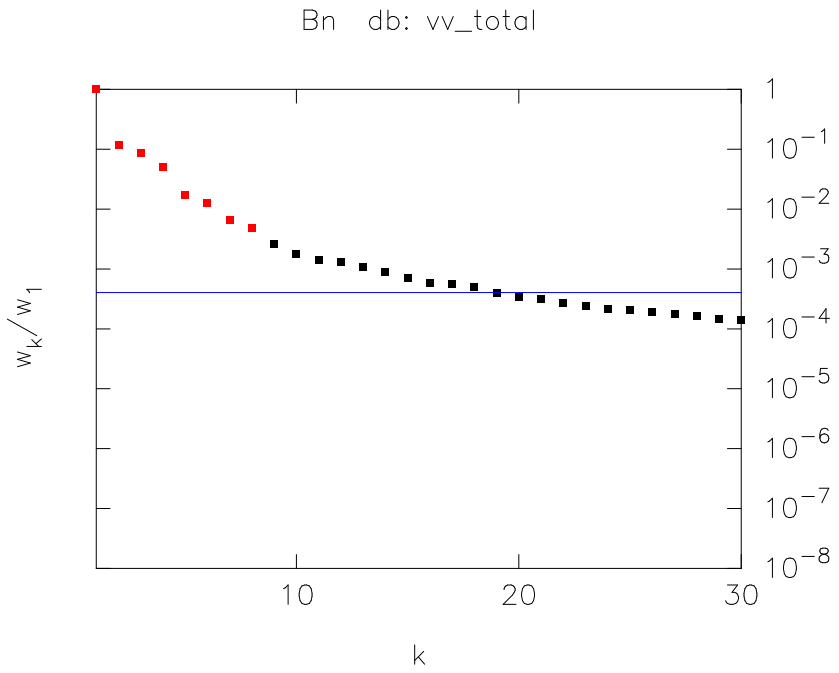

FIG. 4: Singular values for B_n^{tot}, the normal component of total magnetic field on the vacuum vessel. The distribution of singular values is much broader than for the external field analysis; nineteen singular values lie above the 1 Gauss horizontal line.

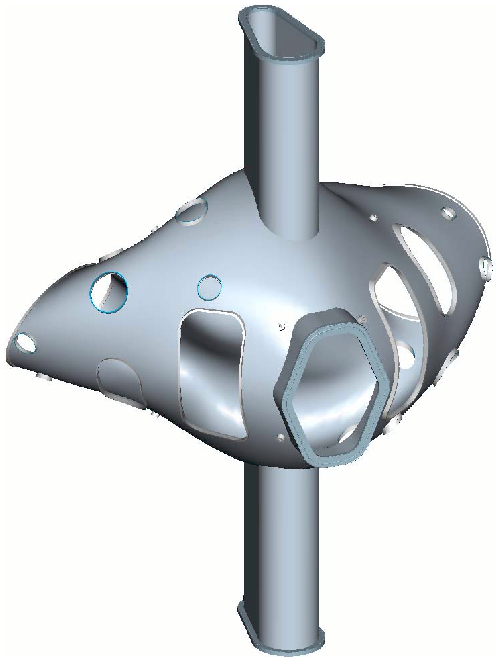

FIG. 5: 3-D view of one period of the NCSX VV

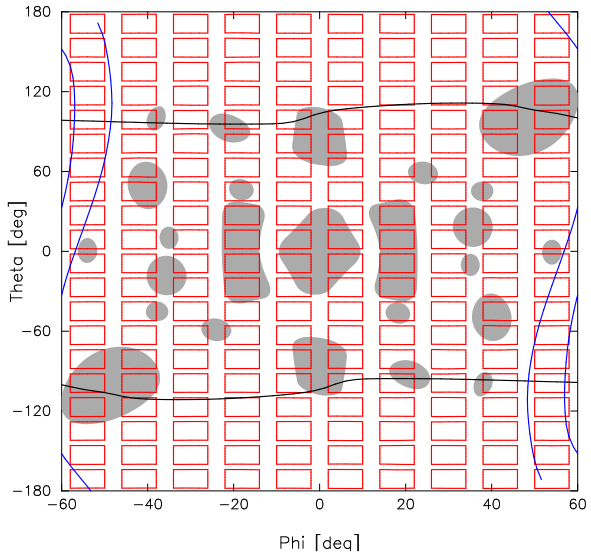

FIG. 6: 200 trial loops in a $\theta - \phi$ representation of one period of the NCSX VV. Only 100 loops in one half-period are unique. Port regions are shaded grey. Curves which traverse the figure in ϕ represent the top and bottom of the VV. Curves which traverse the figure in θ identify the edges of spacer collars which connect adjacent VV periods.

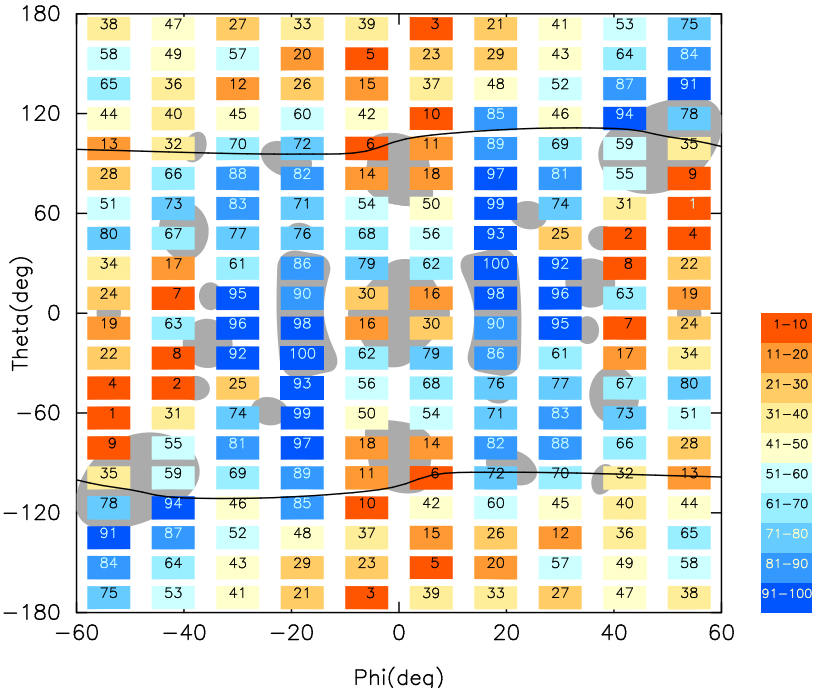

FIG. 7: (Color) Final seedings for the trial set of flux loops in one period of VV-TS.

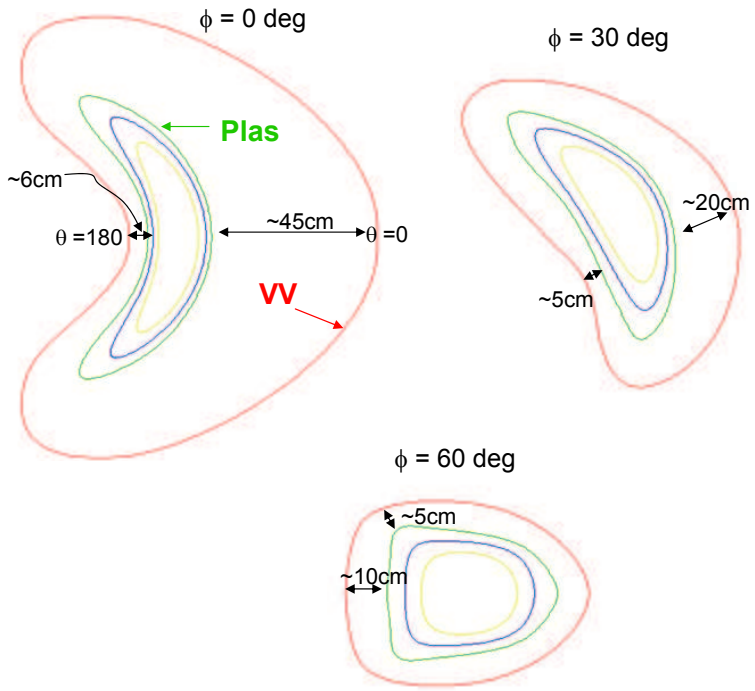

FIG. 8: VV to plasma separation distances, d_{sep}, at various toroidal cross sections.

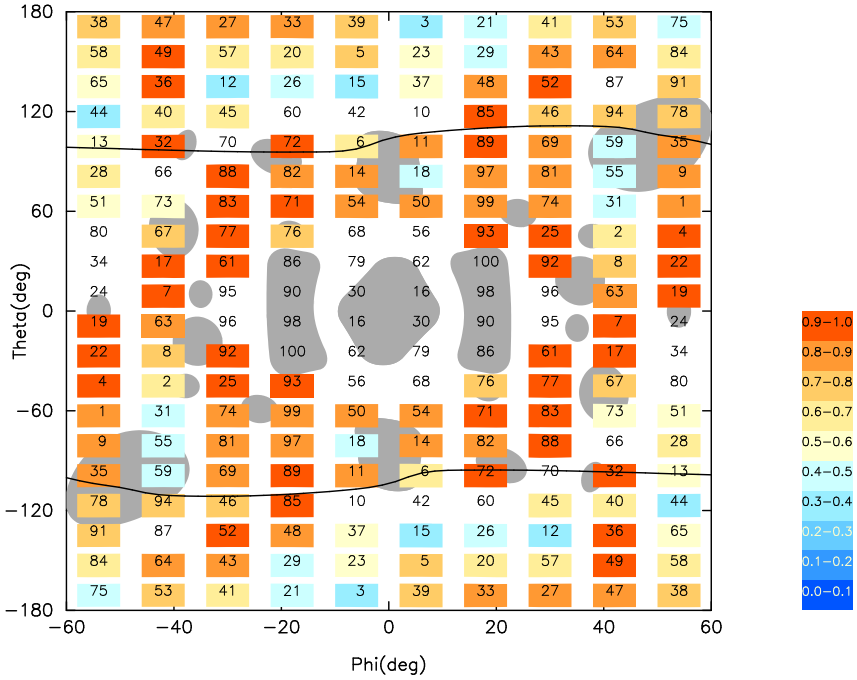

FIG. 9: (Color) Color coded plot of the ratio of (average plasma)/(average total) normal field measured by each of the trial flux loops. A loop is color filled according to the value of the ratio, but only if the average plasma signal exceeds 100 Gauss. In all cases the numerical value of loop seeding is shown.

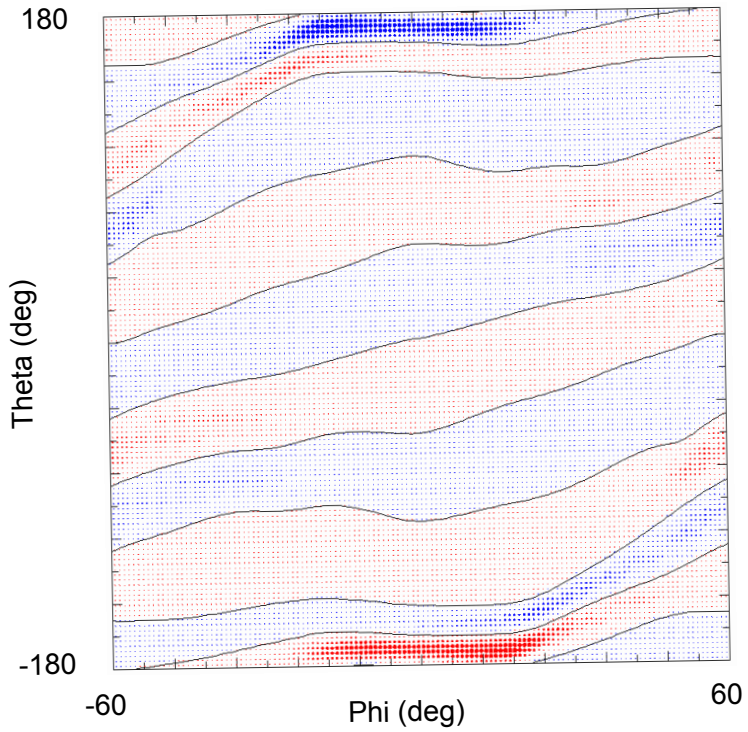

FIG. 10: (Color) Dipole excitation plot showing effectiveness of a distribution of dipoles on the VV in detecting an island on a chosen rational surface in the plasma ($m = 5, n = 3$ corresponding to iota = 0.6). Contours of $B_{53} = 0$ are also shown.

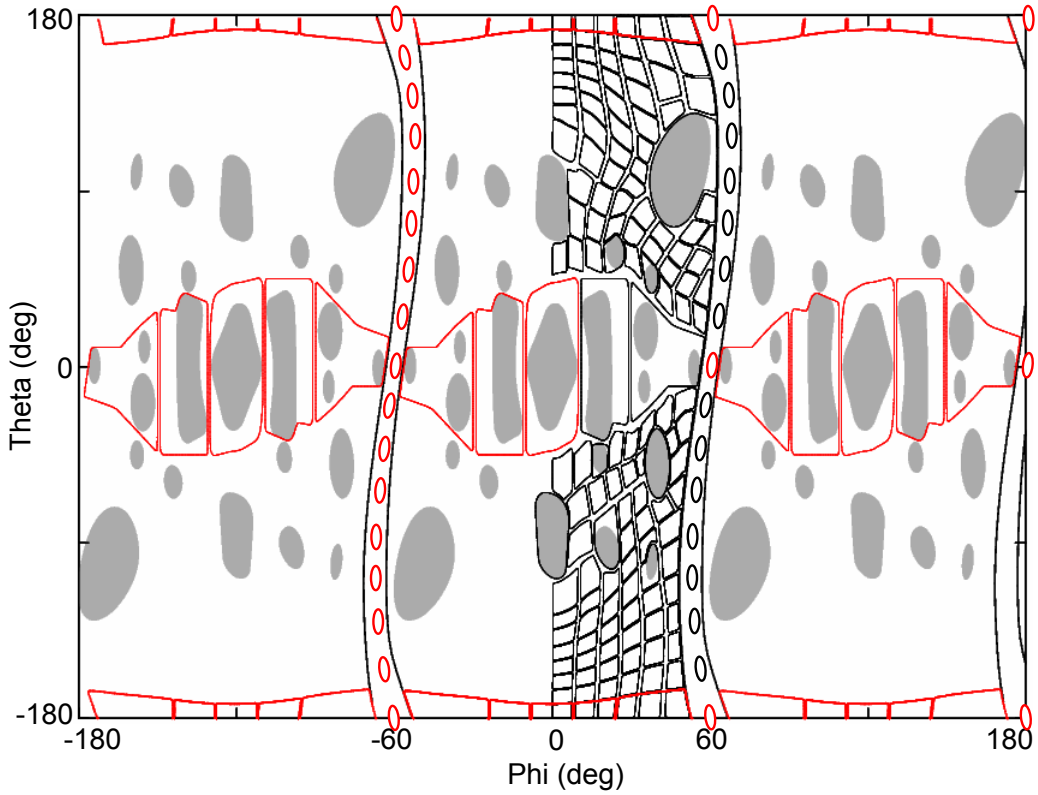

FIG. 11: (Color) Full torus display of intermediate NCSX flux loop design, confining SS mode detection loops (shown in black) to a single half period. Loops in red are for NSS mode detection.

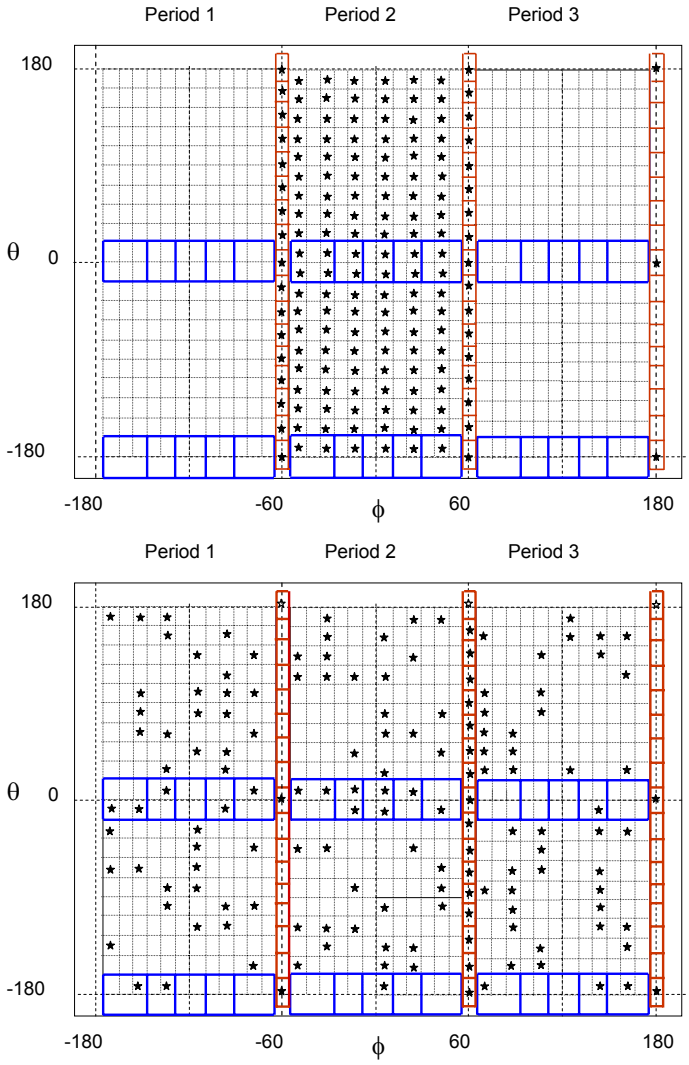

FIG. 12: (Color) Top: Columnar 1-period distribution of trial loops; Bottom: Random in full torus distribution of trial loops, constrained to sample each of the SS loop positions at least once.

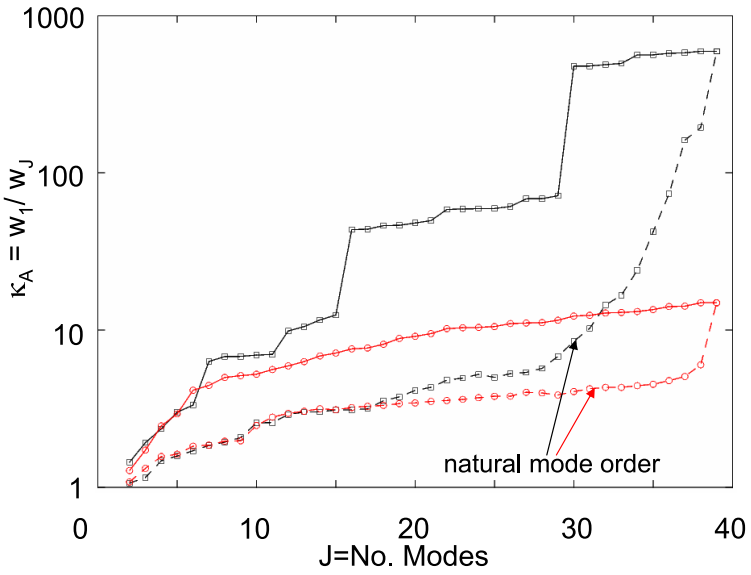

FIG. 13: (Color) Condition number, κ_A, versus number of modes included. Black curves correspond to columnar distribution of loops shown in top frame of Fig. 12; Red curves correspond to the irregular distribution of loops over the full torus (bottom frame of Fig. 12).

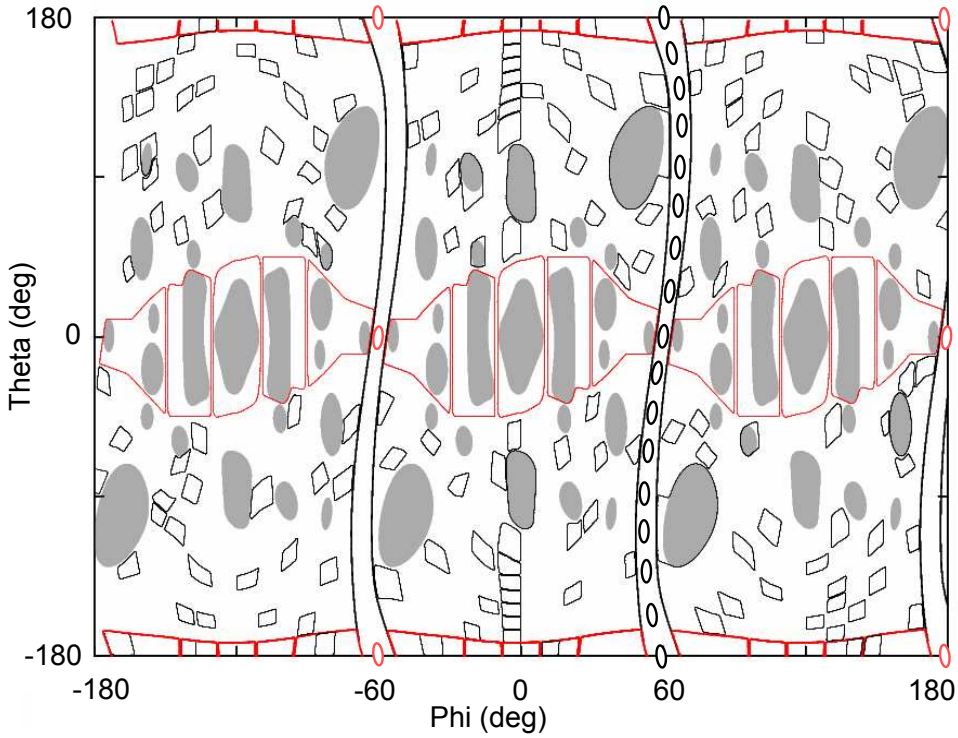

FIG. 14: (Color) Final design for NCSX flux loops. Loops distributed over full torus to improve ability to diagnose non-stellarator symmetric fields without compromising ability to diagnose stellarator symmetric fields.

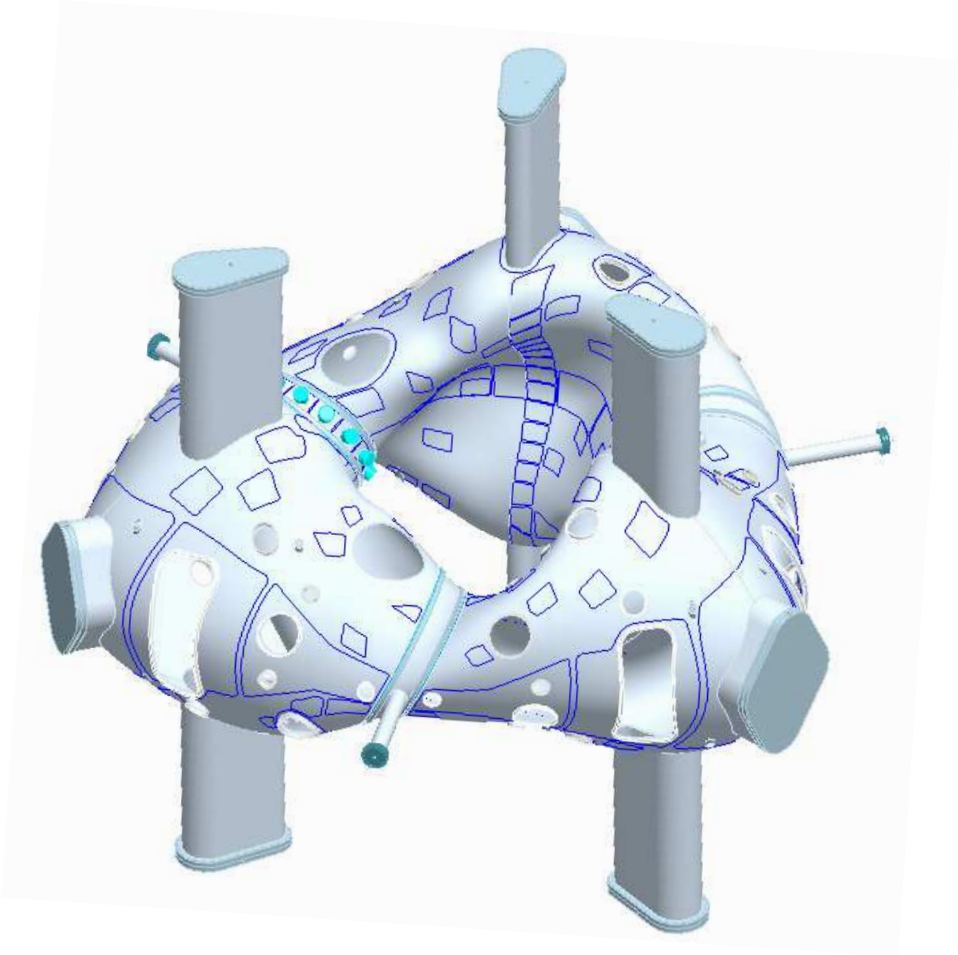

FIG. 15: A 3-D view of the NCSX Vacuum Vessel showing the final flux loop design

The Princeton Plasma Physics Laboratory is operated
by Princeton University under contract
with the U.S. Department of Energy.

Information Services
Princeton Plasma Physics Laboratory
P.O. Box 451
Princeton, NJ 08543

Phone: 609-243-2750
Fax: 609-243-2751
e-mail: pppl_info@pppl.gov
Internet Address: http://www.pppl.gov